

Cluster correlation and nuclear vorticity in low-lying 1^- states of ^{24}Mg

Yohei Chiba 

*Department of Physics, Osaka City University, Osaka 558-8585, Japan;
Nambu Yoichiro Institute of Theoretical and Experimental Physics, Osaka City University, Osaka 558-8585, Japan;
and Research Center for Nuclear Physics (RCNP), Osaka University, Ibaraki 567-0047, Japan*

Yoshiko Kanada-En'yo and Yuki Shikata

Department of Physics, Kyoto University, Kyoto 606-8502, Japan



(Received 3 October 2019; revised 1 May 2020; accepted 30 June 2020; published 11 June 2021)

Background: Low-energy dipole states have been popular topics in studies of stable and unstable nuclei. In ^{24}Mg , two low-energy dipole modes, the toroidal and compressional states have been theoretically proposed recently. The former state has been associated with cluster structure, but there is no explicit analysis of the cluster structure.

Purpose: Our purpose is to investigate low-lying 1^- states in ^{24}Mg and clarify their properties such as the dipole transition strengths, nuclear vorticity, and cluster features.

Method: Wave functions of 1^- states of ^{24}Mg are described within the antisymmetrized molecular dynamics framework combined with the generator coordinate method. Excitation energies and dipole transition strengths are calculated. Cluster wave functions are explicitly taken into account to reveal the role of cluster correlations in 1^- states. Intrinsic matter density and transition current density are analyzed.

Results: Two low-lying dipole states, the $1_{K=1}^-$ and $1_{K=0}^-$, are obtained. The $1_{K=1}^-$ state has the strongest isoscalar toroidal dipole strength and shows two-vortex structure in the intrinsic transition current density. The $1_{K=0}^-$ state features the isoscalar compressional dipole strength and exhibits the $^{16}\text{O} + ^8\text{Be}$ cluster correlation.

Conclusions: The toroidal and compressional dipole modes separately appear as $K = 1$ and $K = 0$ states in the deformed ^{24}Mg system. The $1_{K=1}^-$ state is the toroidal dipole state with the strong nuclear vorticity but no prominent cluster structure, and the $1_{K=0}^-$ state is the compressional dipole state having enhanced cluster structure but weaker vorticity.

DOI: [10.1103/PhysRevC.103.064311](https://doi.org/10.1103/PhysRevC.103.064311)

I. INTRODUCTION

Isoscalar (IS) monopole and dipole excitations have been extensively investigated by α inelastic scattering experiments. Significant low-energy IS strengths have been observed in various nuclei and are attracting great interest (see, for example, Refs. [1–3] and references therein). A central issue is determining the properties and origins of those low-energy dipole modes.

In order to understand the low-energy dipole modes, the vortical dipole mode (also called the torus or toroidal mode) had been originally proposed by hydrodynamical models [4,5] and later studied with microscopic frameworks such as mean-field approaches [2,6–13], antisymmetrized molecular dynamics (AMD) [14–16], and cluster models [17]. The vortical dipole mode is characterized by the vorticity of the transition current and strongly excited by the toroidal dipole (TD) operator, as discussed by Kvasil *et al.* [9]. These features are different from the compressional dipole (CD) mode, which is excited by the standard IS dipole operator. Following Ref. [9], we call the vortical dipole mode the “TD mode” to distinguish it from the compressional dipole (CD) mode. The TD mode in deformed nuclei has been recently investigated

in various stable and unstable nuclei in a wide mass number region from light- to heavy-mass nuclei. Cluster structures of the TD mode in p -shell nuclei such as ^{12}C and ^{10}Be have been studied [14,15,17].

Very recently, Nesterenko *et al.* have investigated dipole excitations in ^{24}Mg with the Skyrme quasiparticle random phase approximation (QRPA) for axially symmetric deformed nuclei, and they predicted that a TD state appears as the low-lying $K^\pi = 1^-$ state [13]. In the nuclear current density of the TD mode, they found the vortex-antivortex type nuclear current in the deformed system and suggested its association with the cluster structure of ^{24}Mg .

For cluster structures of ^{24}Mg , one of the authors and his collaborators have studied positive-parity states of ^{24}Mg within the AMD framework [18–21] and discussed roles of the cluster structures of $^{20}\text{Ne} + \alpha$, $^{16}\text{O} + ^8\text{Be}$, and $^{12}\text{C} + ^{12}\text{C}$ in the IS monopole excitations [22]. Kimura *et al.* have investigated negative-parity states of ^{24}Mg with the AMD, and discussed triaxial deformations of the ground and negative-parity bands [23].

Our aim is to clarify the properties of the low-lying dipole modes in ^{24}Mg such as vortical and cluster features as well as the IS dipole transition strengths. In order to describe dipole

excitations, we apply the constraint AMD method combined with the generator coordinate method (GCM). As for the constraint parameters for basis wave functions in the AMD + GCM, the quadrupole deformations ($\beta\gamma$) [23,24] and the intercluster distance (d) [25] are adopted. This method is useful to analyze cluster correlations as well as intrinsic deformations because various cluster structures are explicitly taken into account in the d -constraint wave functions as proved with regard to ^{28}Si in Ref. [26], which discussed the role of cluster structure in IS monopole and dipole excitations. In order to investigate properties of the low-lying 1^- states of ^{24}Mg , the transition strengths are calculated for the TD and CD operators which can probe the vortical and compressional features, respectively. Nuclear vorticity is discussed in our analysis of the intrinsic transition current density. Cluster correlations in the low-lying dipole excitations are also discussed.

The paper is organized as follows. In Sec. II, the framework of AMD+GCM with $\beta\gamma$ and d constraints are explained. Section III shows the calculated results for basic properties of the dipole states, and Sec. IV gives detailed analysis that focuses on the vortical and cluster features. Finally, the paper is summarized in Sec. V. In the Appendix, definitions of the transition current density, dipole operators, and transition strengths are explained.

II. FRAMEWORK

We briefly explain the present framework of the AMD+GCM method with the $\beta\gamma$ and d constraints. The method is similar to that used in Ref. [26]. For details, readers are directed to Refs. [21,23–27] and references therein.

A. Hamiltonian and variational wave function

The microscopic Hamiltonian for an A -nucleon system is given as

$$H = \sum_i^A t_i - t_{\text{c.m.}} + \sum_{i<j}^A v_{ij}^{NN} + \sum_{i<j}^A v_{ij}^{\text{Coul}}. \quad (1)$$

Here, the first term is the kinetic energy, and the center-of-mass kinetic energy $t_{\text{c.m.}}$ is subtracted. For the effective nuclear interaction v_{ij}^{NN} , we employ Gogny D1S interaction [28]. The Coulomb interaction v_{ij}^{Coul} is approximated by a sum of seven Gaussians.

The intrinsic wave function of AMD is given by a Slater determinant of single-nucleon wave functions φ_i ,

$$\Phi_{\text{int}} = \mathcal{A}\{\varphi_1\varphi_2 \dots \varphi_A\}, \quad (2)$$

$$\varphi_i = \phi_i(\mathbf{r})\chi_i\xi_i, \quad (3)$$

$$\phi_i(\mathbf{r}) = \exp\left\{-\sum_{\sigma=x,y,z} v_\sigma \left(r_\sigma - \frac{Z_{i\sigma}}{\sqrt{v_\sigma}}\right)^2\right\}, \quad (4)$$

$$\chi_i = a_i\chi_\uparrow + b_i\chi_\downarrow, \quad (5)$$

where χ_i is the spin part and ξ_i is the isospin part fixed to be proton or neutron. In the present version of AMD, the spatial part $\phi_i(\mathbf{r})$ is expressed by the deformed Gaussian wave packet located at $\mathbf{Z}_i/\sqrt{v_\sigma}$ in the phase space with the width param-

eters v_σ ($\sigma = x, y, z$), which are common for all nucleons, and the spin part is expressed by a_i and b_i . Here \mathbf{Z}_i , a_i , and b_i are complex valuables and v_σ are real valuables.

The Gaussian center parameter (\mathbf{Z}_i), the nucleon-spin direction (a_i and b_i) for each nucleon, and the width parameters v_σ are the variational parameters optimized by the energy variation [27]. The energy variation is performed for the parity-projected intrinsic wave function $\Phi^\pi = \frac{1+\pi P_z}{2} \Phi_{\text{int}}(\pi = \pm)$.

For the ground state, constraint of the quadrupole deformation ($\beta\gamma$ constraint) is imposed in the energy variation of the positive-parity wave function. We use the parametrization β and γ of the triaxial deformation as described in Ref. [27] and get the $\beta\gamma$ -deformed configuration for given β and γ values after the energy variation. For 1^- states, the $\beta\gamma$ -constraint energy variation is performed for the negative-parity wave function. In addition, cluster configurations are also obtained by constraint on the intercluster distance (d constraint) in the energy variation of the negative-parity wave function, and they are combined with the $\beta\gamma$ -deformed configurations. For the cluster configurations, we adopt *quasiclusters* proposed in Ref. [25]. Let us consider $C_1 + C_2$ configuration consisting of two quasiclusters C_1 and C_2 with the mass numbers A_1 and A_2 ($A_1 + A_2 = A$), respectively. Each quasicluster C_j is defined as the A_j -nucleon group consisting of given numbers of neutrons and protons. We select particular A_j nucleons from A nucleons to form the quasicluster and define the intercluster distance $d_{A_1+A_2}$ between the quasiclusters C_1 and C_2 as

$$d_{A_1+A_2} = |\mathbf{R}_{C_1} - \mathbf{R}_{C_2}|, \quad (6)$$

$$(\mathbf{R}_{C_j})_\sigma = \frac{1}{A_j} \sum_{i \in C_j} \text{Re} \left[\frac{Z_{i\sigma}}{\sqrt{v_\sigma}} \right], \quad (7)$$

where \mathbf{R}_{C_j} is the center-of-mass position of the quasicluster C_j . In the d -constraint AMD, the constraint is imposed on the intercluster distance $d_{A_1+A_2}$. We here adopt the $^{20}\text{Ne} + \alpha$, $^{16}\text{O} + ^8\text{Be}$, and $^{12}\text{C} + ^{12}\text{C}$ configurations for $C_1 + C_2$ of quasiclusters with the mass numbers $A_1 + A_2 = 20 + 4$, $16 + 8$, and $12 + 12$, respectively.

After the energy variation under each constraint of (β, γ), d_{20+4} , d_{16+8} , and d_{12+12} , we obtain the basis wave functions optimized for various values of the constraint parameters and superpose them in the GCM calculation, as explained later. For simplicity, we number the obtained basis wave functions $\{\Phi^\pi(m)\}$ with the index m .

It should be stressed that the cluster wave function in the present framework is composed of not inert (frozen) clusters but quasiclusters, which can contain cluster breaking effects such as the core polarization, dissociation, and excitation. These effects are taken into account in the energy variation at a given value of the quasicluster distance $d_{A_1+A_2}$. Moreover, in the small distance limit, the cluster wave function becomes equivalent to a deformed mean-field wave function because of the antisymmetrization of nucleons. Along the distance parameter $d_{A_1+A_2}$, the d -constraint wave function describes the structure change from the one-center system of a mean-field configuration to the two-center system of the spatially

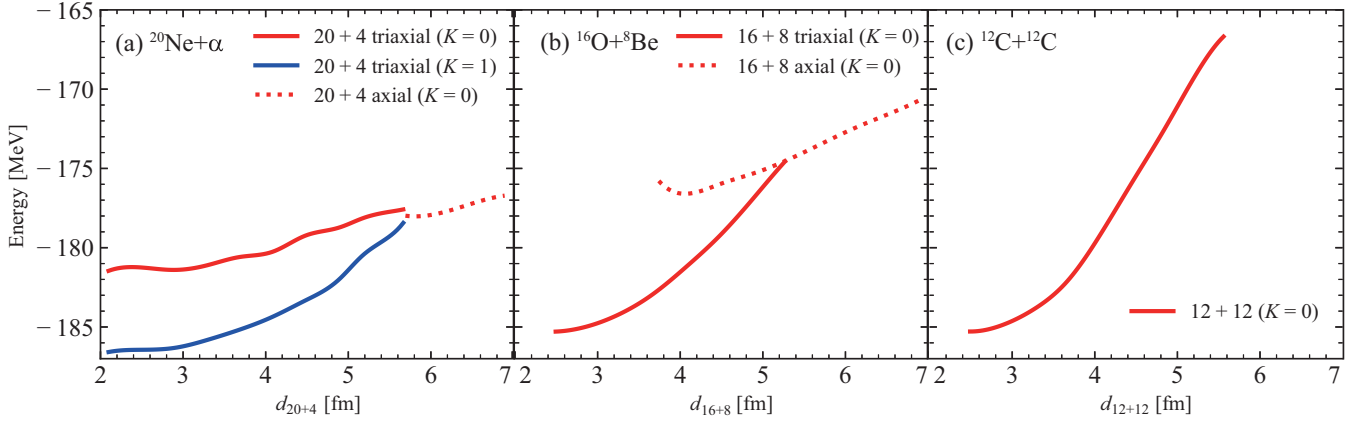


FIG. 1. Energy curves for $^{20}\text{Ne}+\alpha(20+4)$, $^{16}\text{O}+^8\text{Be}(16+8)$, and $^{12}\text{C}+^{12}\text{C}(12+12)$ quasycluster configurations obtained by the d -constraint energy variation for negative-parity states. The $J^\pi = 1^-$ projected energies are plotted as functions of the quasycluster distances $d_{A_1+A_2}$. (a) $^{20}\text{Ne}+\alpha(20+4)$ configuration: energies of $K=0$ and $K=1$ states projected from triaxially deformed intrinsic states and $K=0$ states projected from axially deformed intrinsic states. (b) $^{16}\text{O}+^8\text{Be}(16+8)$ configuration: energies of $K=0$ states projected from triaxially deformed intrinsic states and those projected from axially deformed intrinsic states. (c) $^{12}\text{C}+^{12}\text{C}(12+12)$ configuration: energies of $K=0$ states.

developed $C_1 + C_2$ clustering via intermediate configurations with cluster correlation (or formation) at the nuclear surface.

B. Angular momentum projection and generator coordinate method

After the energy variation with the constraints, the obtained basis wave functions are projected to the angular momentum eigenstates,

$$\Phi_{MK}^{J^\pi}(m) = \frac{2J+1}{8\pi^2} \int d\Omega D_{MK}^{J^*}(\Omega) R(\Omega) \Phi^\pi(m), \quad (8)$$

where $D_{MK}^J(\Omega)$ and $R(\Omega)$ are Wigner's D function and the rotation operator, respectively. They are superposed to describe the final GCM wave function for the J_n^π state,

$$\Psi_{M,n}^{J^\pi} = \sum_{K,m} c_n(K,m) \Phi_{MK}^{J^\pi}(m). \quad (9)$$

Here the coefficients $c_n(K,m)$ are determined by diagonalization of the norm and Hamiltonian matrices so as to satisfy Hill-Wheeler (GCM) equation [29,30].

III. RESULTS

A. Properties of basis wave functions

We describe properties of the $\beta\gamma$ -deformed and cluster configurations obtained by the energy variation with the corresponding constraint.

For the $\beta\gamma$ -deformed configurations, we obtain almost the same results as those in the previous AMD study [23]. In the J^π -projected energy surface on the β - γ plane obtained from the $\beta\gamma$ -deformed configurations, we find the energy minimum state with triaxial deformation at $(\beta, \gamma) = (0.49, 13^\circ)$ for $J^\pi = 0^+$ and that at $(\beta, \gamma) = (0.5, 25^\circ)$ for $J^\pi = 1^-$. These deformed states at the energy minimums become the dominant component of the 0^+_1 and 1^-_1 states in the final result of the GCM calculation.

For the cluster configurations, we adopt the $^{20}\text{Ne}+\alpha$, $^{16}\text{O}+^8\text{Be}$, and $^{12}\text{C}+^{12}\text{C}$ quasyclusters, as described previously. The calculated $J^\pi = 1^-$ energies are shown as functions of quasycluster distances in Fig. 1, and intrinsic density distributions are displayed in Fig. 2.

For the $^{20}\text{Ne}+\alpha(20+4)$ quasycluster configuration, the energy curves are shown in Fig. 1(a) and the density distributions at $d_{20+4} = 2.5, 4.9,$ and 5.9 fm are shown in Figs. 2(a)–2(c). In the $2.0 \leq d_{20+4} \leq 5.7$ fm region, the triaxially deformed $^{20}\text{Ne}+\alpha$ configurations are obtained by the d -constraint energy variation and they yield the $K=0$ and $K=1$ states by the $J^\pi = 1^-$ projection. The $K=1$ energy curve is always lower than the $K=0$ energy curve. The energy difference between the $K=1$ and $K=0$ states is about

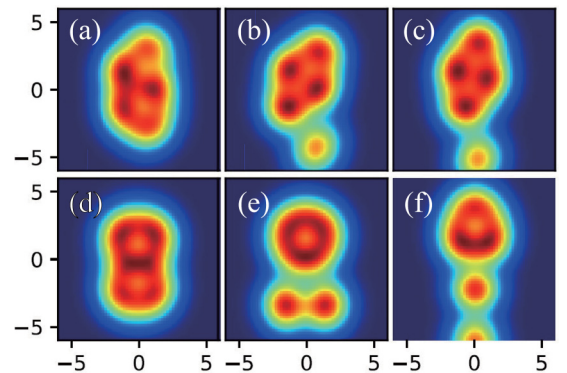


FIG. 2. Intrinsic matter density distributions of the $^{20}\text{Ne}+\alpha$ and $^{16}\text{O}+^8\text{Be}$ quasycluster configurations obtained by the d -constraint energy variation for negative-parity states. Panels (a), (b), and (c) show the $^{20}\text{Ne}+\alpha$ configurations at $d_{20+4} = 2.5, 4.9,$ and 5.9 fm. Panels (d), (e), and (f) show the $^{16}\text{O}+^8\text{Be}$ configurations at $d_{16+8} = 2.5, 4.9,$ and 6.1 fm. The densities sliced at the $x=0$ plane (y - z plane) are shown. The units of the horizontal (y) and vertical (z) axes are fm.

6 MeV at $d_{20+4} = 2.0$ fm but it decreases to approximately 0 MeV at $d_{20+4} = 5.7$ fm. In $d_{20+4} \geq 5.7$ fm region, almost axial symmetric states with the dominant $K = 0$ component are obtained for the $^{20}\text{Ne} + \alpha$ configuration [see Fig. 2(c) and the dotted line of Fig. 1(a)]. It should be noted that $K \neq 0$ components are given only by deviation from the axial asymmetry because of the fact that a complete axial symmetric state is a pure $K = 0$ state.

Figures 1(b) and 2(d)–2(f) show the energy curves and intrinsic density distributions for the $^{16}\text{O} + ^8\text{Be}(16 + 8)$ quasicluster configuration. In $d_{16+8} < 5.4$ fm region, the lowest $^{16}\text{O} + ^8\text{Be}$ configuration is the triaxially deformed configuration because of two α clusters oriented along the y axis as shown in the intrinsic densities [Figs. 2(d) and 2(e)]. It contains only the $K = \text{even}$ component because of the reflection symmetry with respect to π rotation around the z (longitudinal) axis. In the $d_{16+8} \geq 5.4$ fm region, the axially symmetric $^{16}\text{O} + ^8\text{Be}$ configuration [Fig. 2(f)] becomes the lowest, as shown by the dotted line of Fig. 1(b).

In both $^{20}\text{Ne} + \alpha$ and $^{16}\text{O} + ^8\text{Be}$ configurations, the intrinsic wave functions in the small quasicluster distance ($d_{A_1+A_2}$) region show no prominent cluster structure but have large overlap with the $\beta\gamma$ -deformed configuration with triaxial deformations. As the distance $d_{A_1+A_2}$ increases, the energies of the $^{20}\text{Ne} + \alpha$ and $^{16}\text{O} + ^8\text{Be}$ configurations increase gradually, indicating that the system is soft against spatial development of the cluster structures. Compared with the $^{20}\text{Ne} + \alpha$ and $^{16}\text{O} + ^8\text{Be}$ configurations, the energy of the $^{12}\text{C} + ^{12}\text{C}$ configuration increases rapidly as d_{12+12} increases, as shown in Fig. 1(c), because the symmetric cluster configuration is relatively unfavored in the negative-parity ($K^\pi = 0^-$) state. As a result, inclusion of $^{12}\text{C} + ^{12}\text{C}$ cluster configurations gives almost no contribution to the low-lying 1^- states in the GCM calculation.

B. GCM result of dipole excitations

We present the GCM result obtained using all the $\beta\gamma$ deformed and cluster configurations. In the GCM calculation, we take discrete values of generator coordinates as $d_{20+4} = 2.1, 2.3 \dots 6.9$ fm, $d_{16+8} = 2.1, 2.3 \dots 6.9$ fm, and $d_{12+12} = 2.4, 2.6 \dots 5.4$ fm for $J^\pi = 0^+$ and 1^- states. The values of (β, γ) are discretized on a triangular lattice in the β - γ plane with the lattice size of 0.05 and $\beta \leq 0.8$. We focus on the low-lying 1^- states and their isoscalar dipole strengths. The definitions of the CD and TD operators and transition strengths are explained in the Appendix.

1. Spectra and transition strengths

The calculated CD and TD transition strengths [$B(\text{CD})$ and $B(\text{TD})$] are plotted with respect to the 1^- excitation energies (E_x) in Fig. 3. In the low-energy region $E_x \approx 10$ MeV, we obtain two dipole states, the 1^-_1 and 1^-_2 states, which have quite different properties. One is the 1^-_1 state at $E_x = 9.5$ MeV with the strongest TD transition, and the other is the 1^-_2 state at $E_x = 11.2$ MeV with the significant CD transition strength. Therefore, the 1^-_1 state can be regarded as the TD mode, and the 1^-_2 state is the low-lying CD mode.

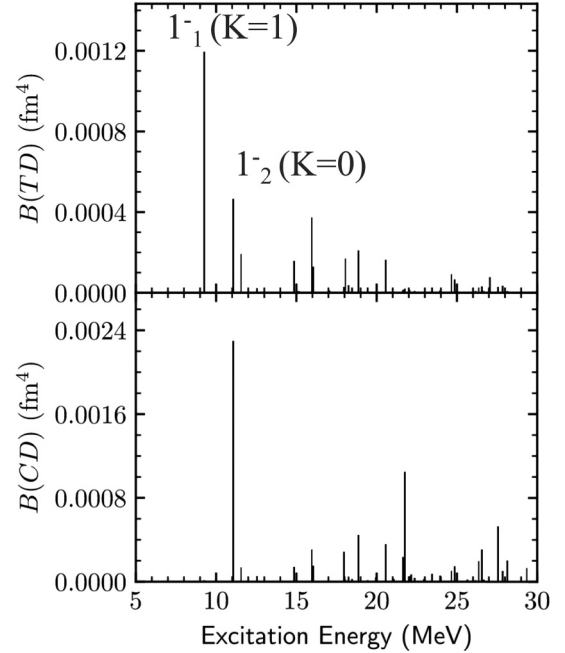


FIG. 3. Strength functions of dipole transitions. The toroidal and compressional dipole strengths, $B(\text{TD})$ and $B(\text{CD})$, are plotted as functions of 1^- excitation energies in the upper and bottom panels, respectively.

In analysis of the dominant K component in these two states, one can assign the former (TD mode) to the bandhead state of a $K = 1$ band and the latter (CD mode) to a $K = 0$ band. This separation of the $K = 1$ and $K = 0$ components in the triaxially deformed intrinsic system plays a key role in the low-lying TD and CD modes in ^{24}Mg . To emphasize this feature of K quanta, we denote the 1^-_1 and 1^-_2 states as $1^-_{K=1}$ and $1^-_{K=0}$, respectively, in the following. The energy ordering of these two 1^- states in our result is consistent with the results of $\beta\gamma$ -AMD [23] and QRP [13] calculations. In the experimental data, 1^- (7.56 MeV) and 1^- (8.44 MeV) states were tentatively assigned to $K = 0$ and $K = 1$, respectively [31]. Therefore, the theoretical $1^-_{K=1}$ and $1^-_{K=0}$ states in the present result may correspond to the experimental 1^- (8.44 MeV) and 1^- (7.56 MeV) states, though the energy ordering of two states seems inconsistent with the observation.

2. Cluster correlations

We here discuss roles of cluster correlations in the $1^-_{K=1}$ and $1^-_{K=0}$ states. To discuss the cluster correlation effect, we perform the GCM calculation using only the $\beta\gamma$ configurations but without the cluster configurations and compare the results with and without cluster configurations. The excitation energies and transition strengths of the $1^-_{K=1}$ and $1^-_{K=0}$ states calculated with and without cluster configurations are summarized in Table I.

The correlation energies induced by the cluster correlations can be evaluated by the energy gain by inclusion of the cluster configurations. The energy gain is 0.3 MeV for the $1^-_{K=1}$ state and 1.0 MeV for the $1^-_{K=0}$ state. The large energy gain in the $1^-_{K=0}$ state indicates significant cluster correlation, which

TABLE I. The calculated values of excitation energies (E_x) and TD and CD strengths of the $1_{K=1}^-$ and $1_{K=0}^-$ states obtained by the GCM calculations with and without the cluster configurations (cc).

	$K = 1$ state		$K = 0$ state	
	With cc	Without cc	With cc	Without cc
E_x (MeV)	9.52	9.85	11.21	12.18
$B(\text{TD})$ (10^{-3} fm 4)	1.20	1.13	0.41	0.32
$B(\text{CD})$ (10^{-3} fm 4)	0.00	0.00	2.38	1.61

mainly comes from the $^{16}\text{O} + ^8\text{Be}$ configuration. The cluster correlation from the $^{16}\text{O} + ^8\text{Be}$ configuration also contributes to the CD transition strength of the $1_{K=0}^-$ state as 50% enhancement of $B(\text{CD})$. This result is understood by the general principle that the low-energy ISD strengths can be enhanced by asymmetric clustering, as discussed in Ref. [32]. Compared with the $1_{K=0}^-$ state, the properties of the $1_{K=1}^-$ state is not affected so much by inclusion of cluster configurations.

IV. DISCUSSION

A. Cluster correlations in $1_{K=1}^-$ and $1_{K=0}^-$

In the previous discussion, we showed that inclusion of cluster configurations gives significant contributions to the $1_{K=0}^-$ state but relatively minor effect on the $1_{K=1}^-$ state. However, it does not necessarily mean no cluster correlation in the $1_{K=1}^-$ state because $\beta\gamma$ -deformed configurations can implicitly contain cluster correlations. We have shown, in the previous analysis including the cluster configurations, the effects from prominent cluster structures which are beyond the $\beta\gamma$ -constraint method.

For more detailed investigation of cluster components in the $1_{K=1}^-$ and $1_{K=0}^-$ states, we calculate overlap of the GCM wave function with each basis of quasicluster configurations. The $1_{K=1}^-$ state has 89% overlap with the $^{20}\text{Ne} + \alpha$ configuration at $d_{20+4} = 2.5$ fm projected to $J^\pi = 1^-(K=1)$, which indicates significant $^{20}\text{Ne} + \alpha$ component. Similarly, the $1_{K=0}^-$ state is dominantly described by $K=0$ component of the $^{16}\text{O} + ^8\text{Be}$ configuration at $d_{16+8} = 2.5$ fm with 88% overlap. The $1_{K=0}^-$ state also has non-negligible overlap with spatially developed $^{16}\text{O} + ^8\text{Be}$ configurations, e.g., 23% overlap

at $d_{16+8} = 4.9$ fm. These developed $^{16}\text{O} + ^8\text{Be}$ cluster components contribute to enhancement of the CD transition strength discussed previously.

B. Vorticity of the nuclear current

In order to reveal vortical nature of the two low-energy dipole modes, we analyze the intrinsic transition current density $\delta\mathbf{j}(\mathbf{r})$ of $0^+_{1} \rightarrow 1_{K=1}^-$ and $0^+_{1} \rightarrow 1_{K=0}^-$ transitions. For simplicity, we take the dominant configuration of each state as an approximate intrinsic state and compute the transition current density in the intrinsic frame: We choose the $\beta\gamma$ -deformed configuration at $(\beta, \gamma) = (0.49, 13^\circ)$ for the ground state, the $^{20}\text{Ne} + \alpha$ configuration at $d_{20+4} = 2.5$ fm for the $1_{K=1}^-$ state, and the $^{16}\text{O} + ^8\text{Be}$ configuration at $d_{16+8} = 2.5$ fm for the $1_{K=0}^-$. In Fig. 4, the transition current density $\delta\mathbf{j}$ and vorticity $\nabla \times \delta\mathbf{j}$ calculated after the parity projection are displayed by vector and color plots, respectively. The intrinsic matter density distribution of the 1^- states before the parity projection is also shown by contour plot.

In the transition current density in the $1_{K=1}^-$ excitation [Figs. 4(a) and 4(c)], one can see two vortices with opposite directions in the upper and lower parts of the longitudinal matter density. The opposite vorticity is a specific character of the vortical dipole mode with $K=1$ in an elongated deformation, and is consistent with the dipole mode called the vortex-antivortex configuration in Ref. [13]. On the other hand, the transition current density in the $1_{K=0}^-$ excitation [Figs. 4(b) and 4(d)] shows no vortex but does show irrotational flow with compressional nature along the z axis (the longitudinal direction), which contributes to the CD dipole strength. The difference in the vortical nature between the $1_{K=0}^-$ and $1_{K=1}^-$ states can be more clearly seen in color plots of the vorticity. The $1_{K=1}^-$ excitation indicates the strong nuclear vorticity in the top and bottom edge parts of the elongated shape, but the $1_{K=0}^-$ excitation shows much weaker vorticity.

C. Cluster and single-particle natures of $1_{K=1}^-$ state

As described previously, the $1_{K=1}^-$ state is approximately described by the $^{20}\text{Ne} + \alpha$ cluster configuration at $d_{20+4} = 2.5$ fm, which does not show a spatially developed clustering but the cluster correlation in the triaxially deformed state. As can be seen in the intrinsic density distribution shown in Fig. 2(a),

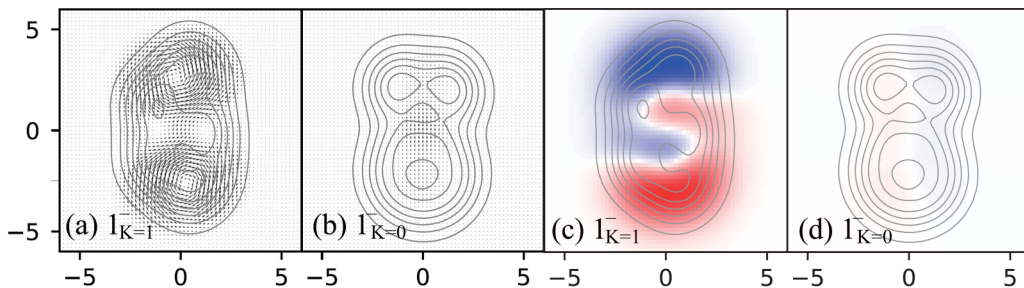


FIG. 4. The intrinsic transition current density $\delta\mathbf{j}(\mathbf{r})$ after the parity projection for $0^+_{1} \rightarrow 1_{K=1}^-$ and $0^+_{1} \rightarrow 1_{K=0}^-$ transitions. In the left and right pairs of panels, the arrows [panels (a) and (b)] and color plots [panels (c) and (d)] indicate $\delta\mathbf{j}(\mathbf{r})$ and the x component of the vorticity $\nabla \times \delta\mathbf{j}(\mathbf{r})$, respectively. The contours are intrinsic matter densities of the $1_{K=1}^-$ and $1_{K=0}^-$ states before the parity projection. The densities sliced at $x=0$ plane (y - z plane) are shown. The units of the horizontal (y) and vertical (z) axes are fm.

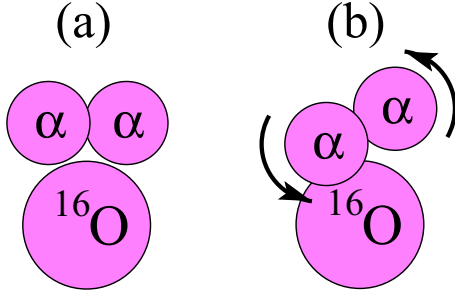


FIG. 5. Schematic figure of $^{16}\text{O}+2\alpha$ cluster structure for the (a) ground state and (b) $1_{K=1}^-$ excitation.

the essential cluster correlation in the $1_{K=1}^-$ state is formation of α clusters caused by four nucleon correlations at the nuclear surface. In a schematic picture shown in Fig. 5, the cluster correlation in the $1_{K=1}^-$ state is associated with the ^{16}O core with two α clusters in one side of the core [see Fig. 5(b)]. Two α clusters are placed at the surface of the ^{16}O core in a tilted configuration, which yields the $K = 1$ component because of the asymmetry against the π rotation around the z axis. On the other hand, the ground state has the triaxial deformation because of the 2α correlation aligned in a normal direction along the surface of ^{16}O [see Fig. 5(a)]. Then, the dipole excitation from the ground state to the $1_{K=1}^-$ state can be understood by the vibrational (tilting) motion of the 2α orientation at the surface of the ^{16}O core. This tilting motion of the 2α clustering produces the nuclear vorticity. Then, the vortex is duplicated in both sides because of the antisymmetrization effect and parity projection.

It is also worth mentioning a link between cluster and mean-field pictures for the $1_{K=1}^-$ mode by considering the small limit of the intercluster distance, where the cluster structure can be associated with a deformed harmonic oscillator configuration. We here use the representation $(n_x n_y n_z)$ with oscillator quanta n_σ in σ axis for a single-particle orbit in the deformed harmonic oscillator. In this limit, the ground state corresponds to the $(011)^4(002)^4$ configuration with triaxial deformation, while the $1_{K=1}^-$ state is regarded as $(011)^3(002)^4(003)^1$. It means that the $1_{K=1}^-$ transition is described by one-particle one-hole excitation of $(011)^{-1}(003)^1$ on the triaxially deformed ground state, which induces the vortical nuclear current and contributes to the TD strength. This mechanism is similar to that discussed with the deformed mean-field approach in Ref. [13]. However, we should remark that the present $1_{K=1}^-$ mode contains the cluster correlation and corresponds to the coherent one-particle one-hole excitations in the LS -coupling scheme. The coherent contribution from four nucleons in the $SU(4)$ symmetry (spin-isospin symmetry) enhances collectivity of the vortical dipole excitation further than the jj -coupling configuration.

V. SUMMARY

We investigated the low-lying 1^- states of ^{24}Mg with the AMD+GCM framework with the $\beta\gamma$ constraint for the quadrupole deformation and the d constraint for the $^{20}\text{Ne} + \alpha$, $^{16}\text{O} + ^8\text{Be}$, and $^{12}\text{C} + ^{12}\text{C}$ configurations. We discussed prop-

erties of the 1^- states such as IS dipole transition strengths, cluster correlations, and vortical nature. In the low-energy region $E_x \approx 10$ MeV, we obtained the $1_{K=1}^-$ and $1_{K=0}^-$ states, which show quite different features. The $1_{K=1}^-$ is the toroidal dipole mode, which is characterized by the nuclear vorticity. The $1_{K=0}^-$ state has the significant compressional dipole strength and the weaker vorticity. Effects of the cluster correlations on the excitation energy and transition strength of these two low-lying dipole states were analyzed. It was found that the spatially developed cluster configurations give significant contribution to the $1_{K=0}^-$ state, whereas the effect on the $1_{K=1}^-$ state is minor. We should stress that the deformation and cluster correlations play important roles in the low-energy dipole modes of ^{24}Mg .

ACKNOWLEDGMENTS

The authors thank Prof. Nesterenko and Prof. Kimura for fruitful discussions. Some of the numerical calculations of this work were performed using the supercomputer at Yukawa Institute for Theoretical Physics, Kyoto University. This work was supported by the Ministry of Education, Culture, Sports, Science and Technology (MEXT) and Japan Society for the Promotion of Science (JSPS) for Grants-in-Aid for Scientific Research (Grants No. 16J03654, No. 18K03617, No. 18H05407, No. 18J20926, No. 18H05863, and No. 19K21046).

APPENDIX: DEFINITION OF TRANSITION DENSITIES AND DIPOLE STRENGTHS

The density and current density operators for the nuclear matter are given as follows:

$$\rho(\mathbf{r}) = \sum_k \delta(\mathbf{r} - \mathbf{r}_k), \quad (\text{A1})$$

$$\mathbf{j}(\mathbf{r}) = -\frac{i\hbar}{2m} \sum_k [\nabla_k \delta(\mathbf{r} - \mathbf{r}_k) + \delta(\mathbf{r} - \mathbf{r}_k) \nabla_k]. \quad (\text{A2})$$

For the current density, we consider only the convection term of the nuclear current but not the spin term of magnetization. The transition current density for the transition from the ground (0^+_{11}) to the 1^- states is written as $\langle 1^- | \mathbf{j}(\mathbf{r}) | 0^+_{11} \rangle$.

For the dipole transition strengths, the following CD and TD operators are adopted:

$$M_{\text{CD}}(\mu) = \frac{-i}{2\sqrt{3}c} \int d\mathbf{r} \mathbf{j}(\mathbf{r}) \times \left[\frac{2\sqrt{2}}{5} r^2 \mathbf{Y}_{12\mu}(\hat{\mathbf{r}}) - r^2 \mathbf{Y}_{10\mu}(\hat{\mathbf{r}}) \right], \quad (\text{A3})$$

$$M_{\text{TD}}(\mu) = \frac{-i}{2\sqrt{3}c} \int d\mathbf{r} \mathbf{j}(\mathbf{r}) \times \left[\frac{\sqrt{2}}{5} r^2 \mathbf{Y}_{12\mu}(\hat{\mathbf{r}}) + r^2 \mathbf{Y}_{10\mu}(\hat{\mathbf{r}}) \right], \quad (\text{A4})$$

where $\mathbf{Y}_{\lambda L\mu}$ is the vector spherical harmonics. The CD operator corresponds to the standard IS dipole operator

and is sensitive to the compressional dipole excitations, and the TD operator has been adopted in Ref. [9] as a measure probing the nuclear dipole vorticity. The CD and TD transition strengths are given by the square of the reduced matrix elements of the corresponding dipole operators as $B(\text{CD,TD}; 0^+ \rightarrow 1^-) = |\langle 1^- || M_{\text{CD,TD}} || 0^+ \rangle|^2$. Using the continuity equation, the CD transition strengths is related

to the transition strength for the standard IS dipole operator $M_{\text{IS1}}(\mu) = \int d\mathbf{r} \rho(\mathbf{r}) r^3 Y_{1\mu}(\hat{\mathbf{r}})$ as

$$B(\text{IS1}) \equiv |\langle 1^- || M_{\text{IS1}} || 0^+ \rangle|^2 = \left(\frac{10\hbar c}{E} \right)^2 B(\text{CD}). \quad (\text{A5})$$

-
- [1] M. N. Harakeh and A. van der Woude, *Giant Resonances* (Oxford University Press, Oxford, UK, 2001).
- [2] N. Paar, D. Vretenar, E. Khan, and G. Colo, *Rep. Prog. Phys.* **70**, 691 (2007).
- [3] X. Roca-Maza and N. Paar, *Prog. Part. Nucl. Phys.* **101**, 96 (2018).
- [4] S. F. Semenko, *Sov. J. Nucl. Phys.* **34**, 356 (1981).
- [5] D. G. Ravenhall and J. Wambach, *Nucl. Phys. A* **475**, 468 (1987).
- [6] D. Vretenar, N. Paar, and P. Ring, and T. Nikšić, *Phys. Rev. C* **65**, 021301(R) (2002).
- [7] N. Ryezayeva, T. Hartmann, Y. Kalmykov, H. Lenske, P. von Neumann-Cosel, V. Yu. Ponomarev, A. Richter, A. Shevchenko, S. Volz, and J. Wambach, *Phys. Rev. Lett.* **89**, 272502 (2002).
- [8] P. Papakonstantinou, V. Y. Ponomarev, R. Roth, and J. Wambach, *Eur. Phys. J. A* **47**, 14 (2011).
- [9] J. Kvasil, V. O. Nesterenko, W. Kleinig, P.-G. Reinhard, and P. Vesely, *Phys. Rev. C* **84**, 034303 (2011).
- [10] A. Repko, P.-G. Reinhard, V. O. Nesterenko, and J. Kvasil, *Phys. Rev. C* **87**, 024305 (2013).
- [11] J. Kvasil, V. O. Nesterenko, W. Kleinig, and P.-G. Reinhard, *Phys. Scr.* **89**, 054023 (2014).
- [12] V. O. Nesterenko, J. Kvasil, A. Repko, W. Kleinig, and P.-G. Reinhard, *Phys. At. Nucl.* **79**, 842 (2016).
- [13] V. O. Nesterenko, A. Repko, J. Kvasil, and P. G. Reinhard, *Phys. Rev. Lett.* **120**, 182501 (2018).
- [14] Y. Kanada-En'yo, Y. Shikata, and H. Morita, *Phys. Rev. C* **97**, 014303 (2018).
- [15] Y. Kanada-En'yo and Y. Shikata, *Phys. Rev. C* **95**, 064319 (2017).
- [16] Y. Kanada-En'yo and Y. Shikata, *Phys. Rev. C* **100**, 014301 (2019).
- [17] Y. Shikata, Y. Kanada-En'yo, and H. Morita, *Prog. Theor. Exp. Phys.* **2019**, 063D01 (2019).
- [18] Y. Kanada-En'yo, H. Horiuchi, and A. Ono, *Phys. Rev. C* **52**, 628 (1995).
- [19] Y. Kanada-En'yo and H. Horiuchi, *Phys. Rev. C* **52**, 647 (1995).
- [20] Y. Kanada-En'yo and H. Horiuchi, *Prog. Theor. Phys. Suppl.* **142**, 205 (2001).
- [21] Y. Kanada-En'yo, M. Kimura, and A. Ono, *Prog. Theor. Exp. Phys.* **2012**, 01A202 (2012).
- [22] Y. Chiba and M. Kimura, *Phys. Rev. C* **91**, 061302(R) (2015).
- [23] M. Kimura, R. Yoshida, and M. Isaka, *Prog. Theor. Phys.* **127**, 287 (2012).
- [24] T. Suhara and Y. Kanada-En'yo, *Prog. Theor. Phys.* **123**, 303 (2010).
- [25] Y. Taniguchi, M. Kimura, and H. Horiuchi, *Prog. Theor. Phys.* **112**, 475 (2004).
- [26] Y. Chiba, Y. Taniguchi, and M. Kimura, *Phys. Rev. C* **95**, 044328 (2017).
- [27] M. Kimura, *Phys. Rev. C* **69**, 044319 (2004).
- [28] J. F. Berger, M. Girod, and D. Gogny, *Comput. Phys. Commun.* **63**, 365 (1991).
- [29] D. L. Hill and J. A. Wheeler, *Phys. Rev.* **89**, 1102 (1953).
- [30] J. J. Griffin and J. A. Wheeler, *Phys. Rev.* **108**, 311 (1957).
- [31] L. K. Fifield, E. F. Garman, M. J. Hurst, T. J. M. Symons, F. Watt, C. H. Zimmerman, and K. W. Allen, *Nucl. Phys. A* **322**, 1 (1979).
- [32] Y. Chiba, M. Kimura, and Y. Taniguchi, *Phys. Rev. C* **93**, 034319 (2016).